ACES Asian Chemical Editorial Society

doi.org/10.1002/asia.202300836

CHEMISTRY AN ASIAN JOURNAL Research Article

www.chemasianj.org

# An Experimental and Theoretical Insight into $I_2/Br_2$ Oxidation of Bis(pyridin-2-yl)Diselane and Ditellane

M. Carla Aragoni,[a] Enrico Podda,[a, b] Savita Chaudhary,[c] Aman K. K. Bhasin,[d] Kuldip K. Bhasin,[c] Simon J. Coles,[e] James B. Orton,[e] Francesco Isaia,[a] Vito Lippolis,[a] Anna Pintus,[a] Alexandra M. Z. Slawin,[f] J. Derek Woollins,[f, g] and Massimiliano Arca*[a]

The reactivity between bis(pyridin-2-yl)diselane $^{o}Py_2Se_2$ and ditellane $^{o}Py_2Te_2$ (**L1** and **L2**, respectively; $^{o}Py$ = pyridyn-2-yl) and $I_2/Br_2$ is discussed. Single-crystal structure analysis revealed that the reaction of **L1** with $I_2$ yielded $[(HL1^{+})(I^{-})\cdot 5/2I_2]_{\infty}$ (**1**) in which monoprotonated cations $HL1^{+}$ template a self-assembled infinite *pseudo*-cubic polyiodide 3D-network, while the reaction with $Br_2$ yielded the dibromide $H^{o}PySe^{II}Br_2$ (**2**). The oxidation of **L2** with $I_2$ and $Br_2$ yielded the compounds $H^{o}PyTe^{II}I_2$ (**3**) and $H^{o}PyTe^{IV}Br_4$ (**6**), respectively, whose structures were elucidated by X-ray diffraction analysis. FT-Raman spectroscopy measurements are consistent with a 3c–4e description of all the X–Ch–X three-body systems (Ch = Se, Te; X = Br, I) in compounds **2**, **3**, $H^{o}PyTe^{II}Br_2$ (**5**), and **6**. The structural and spectroscopic observations are supported by extensive theoretical calculations carried out at the DFT level that were employed to study the electronic structure of the investigated compounds, the thermodynamic aspects of their formation, and the role of noncovalent σ-hole halogen and chalcogen bonds in the X···X, X···Ch and Ch···Ch interactions evidenced structurally.

## Introduction

Diaryl-diselenides (diselanes) and ditellurides (ditellanes) $Ar_2Ch_2$ (Ar = aryl group; Ch = Se, Te) featuring a Ch–Ch bond[1] are a well-known class of organic compounds showing a variety of biological and pharmacological applications, in particular due to their antioxidant and prooxidant properties.[2,3] In particular, the prooxidant properties of diselanes could be exploited to target specific redox-sensitive proteins showing different biological activities.[4,5] Recently, diselenides were reported to promote a hormetic effect in different cell lines thanks to the interaction with the free cysteine-thiol of the repressor Kelch-like ECH-associated protein 1 (Keap1).[6] Ditellurides have shown a similar biological activity. For example, bis(cyclodextrinyl)ditelluride was designed to be a functional mimic of glutathione peroxidase,[7,8] and evidence of thiol peroxidase activity of diphenyl ditelluride in mice was reported in recent years.[2,9,10] The redox properties of diaryldichalcogenides, and hence their biological activity, can be modulated by their capability to participate to a variety of weak interactions involving the chalcogen atoms Ch and the substituents Ar.[11] In this context, dichalcogenides $Ar_2Ch_2$ can be oxidized by dihalogens $X_2$ (X = Cl, Br, I) to give a variety of reaction products. The first oxidation step results in the cleavage of the Ch–Ch bond (analogous to Zincke reaction in disulfides for X = Cl, Br)[12] to give neutral arylchalcogenyl halides $ArCh^{II}X$ and/or anionic T-shaped arylchalcogenyl dihalides $[ArCh^{II}X_2]^{-}$. A further oxidation step can lead to discrete arylchalcogenyltetrahalides[13–15] $[ArCh^{IV}X_4]^{-}$ or extended catena-μ-halo-dihalo(aryl)-chalcogen(IV)[15–17] with the chalcogen atom assuming a distorted square-pyramidal geometry. Halides in

[a] Prof. Dr. M. C. Aragoni, Dr. E. Podda, Prof. F. Isaia, Prof. Dr. V. Lippolis, Dr. A. Pintus, Prof. Dr. M. Arca
Dipartimento di Scienze Chimiche e Geologiche
Università degli Studi di Cagliari
S.S. 554 bivio per Sestu, 09042 Monserrato (Cagliari) (Italy)
E-mail: marca@unica.it

[b] Dr. E. Podda
Centro Servizi di Ateneo per la Ricerca (CeSAR)
Università degli Studi di Cagliari
S.S. 554 bivio Sestu, 09042 Monserrato (Cagliari) (Italy)

[c] Dr. S. Chaudhary, Prof. Dr. K. K. Bhasin
Department of Chemistry, Centre for Advanced Studies in Chemistry
Panjab University
Chandigarh, 160014 (India)

[d] Dr. A. K. K. Bhasin
Department of Chemistry
Amity University
Sector 82 A, Mohali, Punjab-140306 (India)

[e] Prof. Dr. S. J. Coles, Dr. J. B. Orton
UK National Crystallography Service
School of Chemistry
Faculty of Engineering and Physical Sciences
University of Southampton
Southampton SO17 1BJ (UK)

[f] Prof. Dr. A. M. Z. Slawin, Prof. Dr. J. D. Woollins
EaStCHEM School of Chemistry
University of St. Andrews
North Haugh, St. Andrews, Fife, KY16 9ST (UK)

[g] Prof. Dr. J. D. Woollins
Department of Chemistry
Khalifa University
Abu Dhabi 127788 (United Arab Emirates)

Supporting information for this article is available on the WWW under https://doi.org/10.1002/asia.202300836

$ArCh^{II}X$, $[ArCh^{II}X_2]^-$, and $[ArCh^{IV}X_4]^-$ species can be displaced by chalcogen donors[18] RCh′ to give a variety of mixed-valence interchalcogen compounds[19] stabilized by $ArCh(X)_n$←Ch′R interactions ($n=0$–3), such as $[PhTe^{II}(S{=}C(NH_2)_2)][PhTe^{IV}I_4]$,[20] often displaying fascinating supramolecular structures based on both chalcogen bond (ChB) and halogen bond (XB) interactions resulting in Ch···Ch′, Ch···X, and X···X contacts. A further example is provided by mesityltellurenyl iodide MesTeI (Mes = 2,4,6-trimethylphenyl), obtained by diiodine oxidation of bis(mesityl)ditellane $Mes_2Te_2$, which was isolated in the neutral 2:1 adducts with 1,1′-bis(3-methyl-4-imidazolin-2-selone)methane and 1,2-bis(3-methyl-4-imidazolin-2-selone)ethane, featuring the linear Se→Te–I moiety.[18] Among the large variety of aryl substituents in $Ar_2Ch_2$, of particular interest is pyridine, due to its ability to form zwitterionic arylchalcogenyl di- and tetra-halides by N-protonation.[21,22] In 1984 the $Cl_2$ and $Br_2$ oxidation of bis(pyridin-2-yl)diselane ($^oPy_2Se_2$, **L1**; $^oPy$ = pyridyn-2-yl)[23] was hypothesized to give $^o$PySeCl and $^o$PySeBr, respectively.[24] It was only in recent years that the dimer of pyridin-2-yl-selenyl chloride $(^oPySeCl)_2$, stabilized by intermolecular N→Se interactions, was isolated along with the T-shaped zwitterionic 1*H*-pyridine-2-selenyl dichloride $H^oPySeCl_2$.[22] Analogously, the dibromine oxidation of compound **L1** in $CH_2Cl_2$ was reported to give the $^o$PySeBr species, isolated but not structurally characterized, which evolved in the stable T-shaped zwitterion $H^oPySeBr_2$ in methanol solution.[25] Curiously, neither $H^oPySeI_2$ nor any $H^oPySeX_4$ species (X = Br, I) have been reported to date.

An analogous reactivity was reported for bis(pyridin-2-yl)ditellane ($^oPy_2Te_2$; **L2**),[26] that provided the dimer $(^oPyTeCl)_2$ and 1*H*-pyridine-2-tellurenyl dichloride $H^oPyTeCl_2$ when reacted with $SO_2Cl_2$ in $CH_2Cl_2$,[21,27] Similar compounds were isolated from the reactions of compound **L2** with $I_2$ and $Br_2$ in $CH_2Cl_2$ solution.[28,29] Among the products, the zwitterions $H^oPyTeX_2$ (X = I, Br) and $H^oPyTeI_4$ were isolated and characterized.[28]

During the past decades, our research group has been studying the reactivity of pnictogen[30,31] and chalcogen donors[18,32,33] with dihalogens, with the aim of investigating the nature of the reaction products,[34,35] their formation mechanism,[36] and the use of vibrational spectroscopy to investigate three-body systems of the type Ch–X–Ch, Ch–X–X, and X–Ch–X.[37] In addition, we have investigated the supramolecular assemblies formed by means of noncovalent interactions, such as halogen bond (XB)[37,38] and chalcogen bond (ChB).[39]

In this paper, we present an in-depth structural, spectroscopic, and theoretical investigation on the products obtained by reacting compounds **L1** and **L2** with $I_2$ and $Br_2$.

## Results and Discussion

Bis(pyridin-2-yl)dichalcogenides **L1** and **L2** were made to react in halogenated solvents or acetonitrile solution with diiodine and dibromine, featuring increasingly oxidizing ability, in different molar ratios (ranging between 1:1 and a large excess of the dihalogen), by slow evaporation of the reaction mixtures or by diffusion of the dihalogen vapors into a solution of the dichalcogenide. The outcome of the reactions was not dependent on the nature of the solvent. When crystals suitable for X-ray diffraction analysis[40] could be collected, they were analyzed by microanalytical (determination of the melting point, elemental analysis) and spectroscopic (FT-IR, FT-Raman) methods. In the following, the reactions of **L1**/**L2** with $I_2$ and $Br_2$ (Scheme 1) will be discussed in relation to the oxidizing ability of the dihalogen.

### Reactions of L1 with $I_2$ and $Br_2$

By slow evaporation of a $CH_2Cl_2$ or $CH_3CN$ solution of **L1** and $I_2$ in 1:3 molar ratio, crystals were collected whose elemental analysis

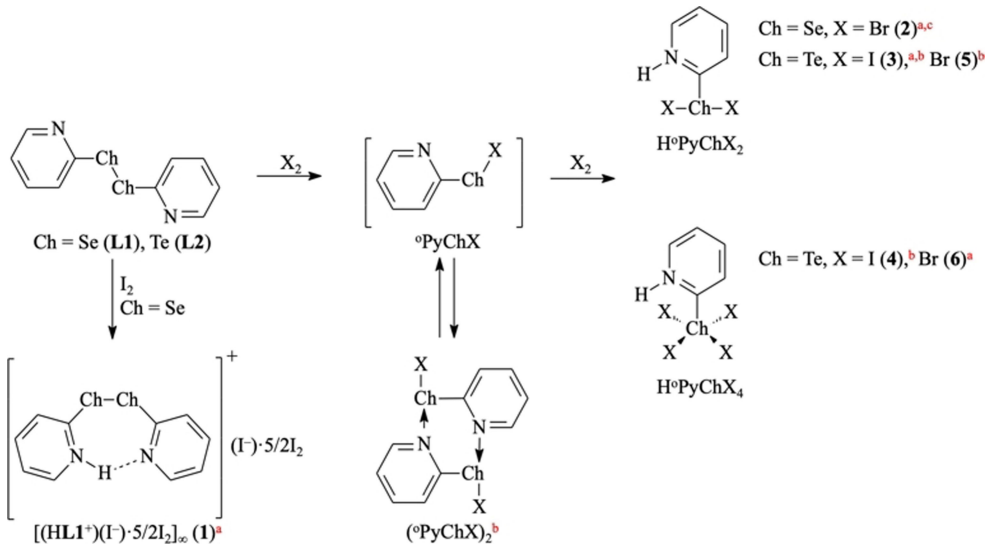


**Scheme 1.** Reaction products isolated from the reactions of **L1** and **L2** with $I_2$ and $Br_2$ (a, this work; b, ref. [28]; c, ref. [25]).

was consistent with the stoichiometry (H**L1**)$I_6$ (**1**; Scheme 1, Tables S1 and S2).[40] The X-ray crystal structure established this compound to be formulated as $[(HL1^+)(I^-)\cdot 5/2I_2]_\infty$, isostructural with $[(HL3^+)(I^-)\cdot 5/2I_2]_\infty$ [**L3** = bis(pyridin-2-yl)disulfide; Figure S1], which in turn was obtained by some of the authors by reacting **L3** and $I_2$ in $CH_2Cl_2$ solution.[33] Regardless of the use of $CH_3CN$ or $CH_2Cl_2$ as a solvent, compound **1** was the sole product obtained and crystallographically characterized from the reaction of **L1** with $I_2$, suggesting a templating key-effect of the N-monoprotonated H**L1**$^+$ cation, featuring a peculiar conformation due to the intramolecular N–H···N hydrogen bond (HB). N-protonation of pyridine derivatives upon reaction with dihalogens or interhalogens has been observed recurrently.[31,41] The oxidation of the aromatic heterocycle to give a cationic radical species followed by solvolysis or reaction with incipient moisture has been proposed as a possible explanation.[31,42] In compound **1**, the N-monoprotonated cations H**L1**$^+$ are arranged in pairs held by couples of almost perfectly linear C6–Se2···Se1$^{i}$ ChBs (Table 1 and Figure 1a). These interactions fall in the category of strong ChBs based on the relative shortening of the Se···Se distance with respect to the sum of the relevant van der Waals radii according to the scale of ChB strength proposed by Aragoni.[39]

The charge of N-monoprotonated cations H**L1**$^+$ is balanced by iodide ions connected by diiodine molecules with all $I^-\cdots I_2$ distances shorter than 3.6 Å,[43,44,45] and therefore forming a self-assembled infinite polyiodide network. Only a limited number of authentic infinite polyiodide three-dimensional frameworks, with all I···I distances shorter than 3.6 Å, such as $[\{Ag([18]aneS_6)\}I_7]$[46] and $[(DMFc)_4I_{26}]$ (DMFc = decamethylferrocene),[47] have been structurally characterized to date. In both cases, distorted polyiodide networks develop around the complex cations, with six diiodine molecules interacting at the iodide anions located at the nodes of the networks in a *pseudo*-octahedral fashion.[46,47] Quite differently, in compound **1** each $I^-$ anion (I1 in Figure 1b), located at the nodes of the network, is secondarily bonded to five $I_2$ molecules in a distorted square-pyramidal fashion at distances ranging between 3.1506(5) and 3.5273(5) Å (Table 1). Each $I_2$ molecule is shared between a pair of symmetry-related $I1^-$ iodides.

The I–I bond lengths in the perturbed diiodine molecules range between 2.7359(4) and 2.7916(5) Å (Table 1), the elongation with respect to the solid-state I–I distance [2.715(6) Å][48] being due to electron density donation from $I^-$ to the σ*-antibonding LUMO of $I_2$. Notably, all the $I^-\cdots I$–I distances fall within the correlation reported by Devillanova[37] typical for $I_A$–$I_B$–$I_C$ three-body systems (Figure 2), which correlates the relative elongations $\delta_1$ and $\delta_2$ of the two interatomic distances $I_A$–$I_B$ and $I_B$–$I_C$ with respect to the sum of the relevant covalent radii (1.33 Å). In particular, the shortest interaction distance $I^-\cdots I_2$ is found in the I1···I2–I3 moiety, which could be considered as a very asymmetric triiodide. The infinite 3D-network is made up of distorted parallelepiped-shaped boxes having iodides at the corners, and $I_2$ or $I_2\cdots I^-\cdots I_2$ units completing the short and long edges, respectively (Figure 3). A central constriction of the parallelepiped-shaped box defines two *pseudo*-cubic chambers hosting two H**L1**$^+$ cations interacting with the polyiodide framework through C1–Se1···I3$^{v}$ ($^{v}$ = 1/2+x, 3/2−y, 1/2+z) and

**Table 1.** Summary of selected distances (*d*, Å) and angles (α, °) of intermolecular chalcogen bond (ChB), halogen bond (XB), and hydrogen bond (HB) interactions for compounds **1**–**6**.

| | Formula | ChB | | | XB | | | HB | | | Ref. |
|---|---|---|---|---|---|---|---|---|---|---|---|
| | | R–Ch···A | $d_{Ch\cdots A}$ | $\alpha_{R-Ch\cdots A}$ | R–X···A | $d_{X\cdots A}$ | $\alpha_{R-X\cdots A}$ | R–H···A | $d_{R\cdots A}$ | $\alpha_{R-H\cdots A}$ | |
| **1** [a] | $[(HL1^+)(I^-)\cdot 5/2I_2]_\infty$ | C6–Se2···Se1$^{i}$ | 3.5560(5) | 177.4(1) | I1···I2–I3 | 3.1506(5) | 178.97(1) | | | | This work |
| | | C1–Se1···I6$^{ii}$ | 3.7713(5) | 174.0(1) | I1···I4–I5 | 3.3040(3) | 169.39(1) | | | | |
| | | Se2–Se1···I3$^{v}$ | 3.8247(5) | 137.26(2) | I1···I5$^{iv}$–I4$^{iv}$ | 3.3424(3) | 168.55(1) | | | | |
| | | Se1–Se2···I4 | 3.6710(5) | 162.84(2) | I1···I6–I6$^{ii}$ | 3.4365(5) | 172.57(1) | | | | |
| | | | | | I1···I3$^{iii}$–I2$^{iii}$ | 3.5273(5) | 160.23(1) | | | | |
| **2** [b] | $HPySeBr_2$ | C1–Se1···Br2$^{i}$ | 3.4326(6) | 172.49(9) | | | | N1–H1···Br1$^{ii}$ | 3.305(3) | 156(4) | [25] |
| **3** [c] | $HPyTe_2$ | C1–Te···I1$^{i}$ | 3.5447(3) | 171.31(6) | | | | N1–H1···I2$^{ii}$ | 3.554(2) | 156(4) | This work |
| **4** [d] | $HPyTeI_4$ | C1–Te1···I2$^{i}$ | 3.966 | 149.6 | Te1–I2F···I2$^{iii}$ | 3.8081(4) | 163.02 | | | | [28] |
| **5** [e] | $HPyTeBr_2$ | C5–Te1···Br4$^{i}$ | 3.6052(4) | 177.98(6) | | | | | | | [28] |
| | | C6–Te2···Br1$^{ii}$ | 3.5930(4) | 178.17(6) | | | | | | | |
| **6** [f] | $HPyTeBr_4$ | C1–Te1···Br1$^{ii}$ | 3.792(1) | 150.3(1) | | | | N1–H1···Br3$^{i}$ | 3.522(7) | 134.1 | This work |
| | | C1–Te1···Br2$^{ii}$ | 3.731(1) | 149.9(1) | | | | | | | |

Symmetry operations: [a] $^{i}$ = 1−x, 1−y, 1−z; $^{ii}$ = −x, 1−y, 1−z; $^{iii}$ = 1/2−x, −1/2+y, 1/2−z; $^{iv}$ = −1+x, y, z; $^{v}$ = 1/2+x, 3/2−y, 1/2+z. [b] $^{i}$ = x, 1/2−y, 1/2+z; $^{ii}$ = 1+x, 1/2−y, 1/2+z. [c] $^{i}$ = 3/2−x, −1/2+y, 1/2−z; $^{ii}$ = x, 1+y, z. [d] $^{i}$ = −1/2+x, 3/2−y, 3/2−z; $^{ii}$ = −1/2+x, y, 3/2−z; $^{iii}$ = 1/2−x, 1/2+y, 1/2+z. [e] $^{i}$ = x, 3/2−y, −1/2+z; $^{ii}$ = x, 3/2−y, −1/2+z. [f] $^{i}$ = 1−x, 1−y, 1−z; $^{ii}$ = x, 1/2−y, 1/2+z.

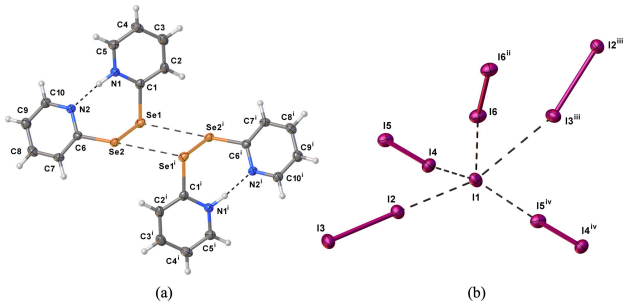


**Figure 1.** Ellipsoid plot and atom labelling scheme of a pair of adjacent interacting HL1$^+$ cations (a) and a portion of the polyiodide network (b) in compound **1**, showing the distorted pentacoordination of the I1 iodide node. Thermal ellipsoids were drawn at the 50% probability level. Selected interatomic distances, angles, and dihedrals: Se1–Se2, 2.3268(5); C1–Se1, 1.920(4); C6–Se2, 1.934(4); Se1···Se2$^{i}$, 3.5560(5); I2–I3, 2.7916(5); I4–I5, 2.7666(3); I6–I6$^{ii}$, 2.7359(4); I1···I2, 3.1506(5); I1···I3$^{iii}$, 3.5273(5); I1···I4, 3.3040(3); I1···I5$^{iv}$, 3.3424(3); I1···I6, 3.4865(5) Å; C1–Se1–Se2, 99.3(1); C6–Se2–Se1, 96.7(1); Se2–Se1···Se2$^{i}$, 97.89(2); Se1$^{i}$···Se2–Se1, 82.11(2); N1–C1–Se1–Se2, 50.7(3); N2–C2–Se2–Se1, 58.2(3)°. Symmetry operations: $^{i}$ = 1−x, 1−y, 1−z; $^{ii}$ = −x, 1−y, 1−z; $^{iii}$ = 1/2−x, −1/2+y, 1/2−z; $^{iv}$ = −1+x, y, z.

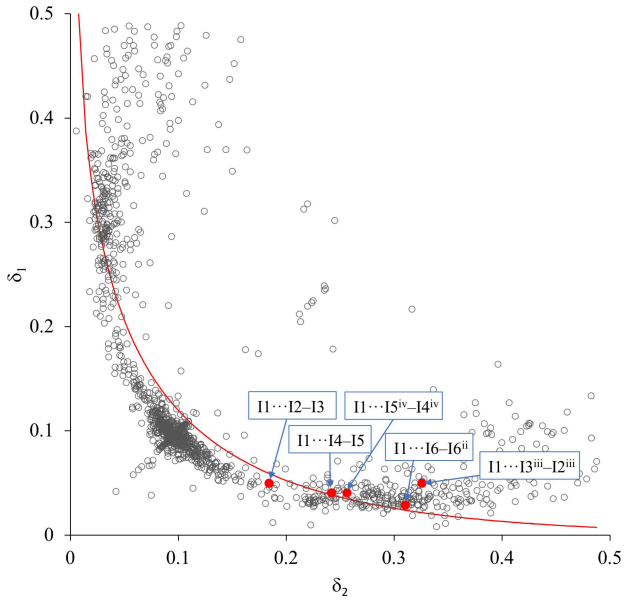


**Figure 2.** Structural data of linear $I_A$–$I_B$–$I_C$ fragments deposited at the CSD reported as scatter plot of $\delta_1$ *vs.* $\delta_2$, where $\delta_1 = \delta(I_A–I_B)$ and $\delta_2 = \delta(I_B–I_C)$. Structural data were taken from ref. [37]. The red dots represent the data for the I$^-$···I–I fragments in the structure of compound **1**. The red solid curve represents the least-squares fit of all data according to the following equation: $\delta_1 = -k \cdot ln[1 - e(-\delta_2/k)]$. Fitted parameter: $k = 0.150$, RMSD = 0.013, normalized RMSD = 0.042.

Se1–Se2···I4 weak ChB interactions (Table 1 and Figure S2). The boxes are orthogonally stacked along the *a*- and *b*-axes, while along *c*, specular boxes are alternated shifted by *b*/2 (Figure S3).

FT-Raman spectroscopy has been largely exploited as a tool to investigate the structure of polyiodides, since it provides information on their $I_2$ and $[I_3]^-$ building blocks.[45] Solid-state $I_2$ shows a peculiar FT-Raman peak at 180 cm$^{-1}$, due to the I–I stretching vibration (I–I bond length = 2.715 Å;[48] bond order $n$ = 1). In I$^-$···I–I systems, the perturbation of the $I_2$ molecule results in a weakening of the I–I bond reflected in an increased interatomic

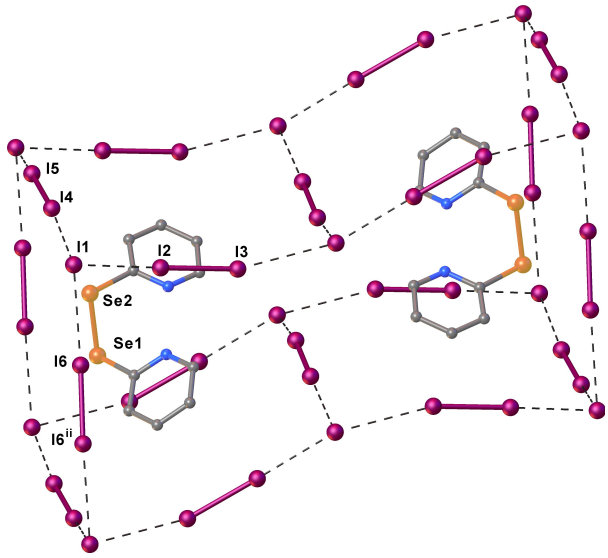


**Figure 3.** Parallelepiped-shaped box generated by the I(1) anions bridged by I(2)–I(3), I(4)–I(5), and I(6)–I(6)$^{ii}$ diiodine molecules hosting the organic HL1$^+$ cations in compound **1**. Hydrogen atoms were omitted for clarity. Symmetry operation: $^{ii}$ = −x, 1−y, 1−z.

distance and a corresponding linearly-dependent shift of the Raman response towards lower wavenumbers.[49] In linear symmetric triiodides (with typical I–I distances in the range 2.90–3.00 Å; $n$ = 0.5), the $\sigma_g$ symmetric stretching vibration can be envisaged in the FT-Raman spectrum at about 110 cm$^{-1}$ ($\nu_{symm}$) while the antisymmetric $\sigma_u$ stretching mode ($\nu_{asymm}$) and the $\pi_u$ bending mode ($\nu_b$) are only IR-active. In asymmetric triiodides (I–I distances in the range 2.80–3.10 Å; $n$ = 0.4–0.6), lacking of an inversion center, the antisymmetric stretching vibration and the bending deformation are also Raman-active, falling at about $\nu_{asymm}$ = 140 and $\nu_b$ = 70 cm$^{-1}$, respectively.[45] In strongly asymmetric triiodides [I···I–I]$^-$ only the peak of the perturbed $I_2$ unit is clearly visible in the range 140–180 cm$^{-1}$, the triiodide peak corresponding to $\nu_{symm}$ becoming very weak if not completely absent.

The FT-Raman spectrum of compound **1** shows a broad peak resulting from the overlapping of three component peaks with maxima at 153, 165, and 178 cm$^{-1}$ (Figure 4), whose wave-

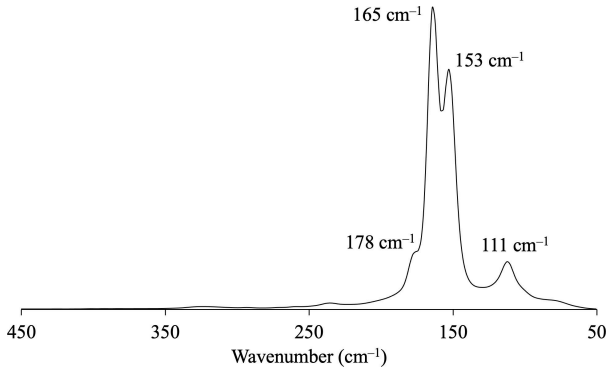


**Figure 4.** Solid-state FT-Raman spectrum (450–50 cm$^{-1}$) recorded at r.t. for compound **1**.

numbers are very close to those previously reported for $[(HL3^{+})(I^{-})\cdot 5/2I_2]_{\infty}$ (156, 166, and 177 $cm^{-1}$).[33] The three components can be assigned, in order of decreasing perturbation of the $I_2$ units, to the stretching vibrations of the perturbed I2–I3, I4–I5, and I6–I6$^{ii}$ diiodine molecules. The very weak peak at 111 $cm^{-1}$ can be assigned to the symmetric stretching mode ($\nu_{symm}$) of the I1···I2–I3 three-body system.

The reactions of **L1** with dibromine in $CH_2Cl_2$ solution yielded red block-shaped crystals suitable for X-ray diffraction analysis, consisting only of the species H°PySeBr$_2$ (**2**; Scheme 1). This compound was previously reported and characterized structurally.[25] It consists of a T-shaped zwitterion with the linear Br–Se–Br moiety, containing a hypercoordinate selenium atom (10–Se–3, according to Arduengo notation),[50] twisted by about 64° with respect to the pyridinium plane. The structural features of the molecular units have already been discussed[25] and they will not be commented further. ChB and HB supramolecular interactions responsible for the crystal packing are summarized in Table 1. The FT-Raman spectrum in the low-energy region can be interpreted based on the structural similarity of the negatively charged Br–Se–Br moiety with the $[Br_3]^{-}$ anion, featuring the symmetric stretching vibration ($\nu_{symm}$) as the only Raman-active mode in the range 160–170 $cm^{-1}$.[30,51] Accordingly, the FT-Raman spectrum of compound **2** is dominated by an intense peak at 161 $cm^{-1}$ (Figure S4), corresponding to the symmetric stretching mode ($\nu_{symm}$) of the linear Br–Se–Br group, while the weak peak at 101 $cm^{-1}$ can be tentatively attributed to the corresponding bending mode ($\nu_b$).

### Reactions of L2 with $I_2$ and $Br_2$

Crystals suitable for X-ray diffraction studies were grown by slow evaporation of a mixture of **L2** with a five-fold excess of $I_2$. An X-ray diffraction analysis carried out at 100 K established the reaction product to consist of H°PyTeI$_2$ (**3**; Scheme 1, Tables S1 and S3), whose structure collected at 298 K was previously published.[28] Under these experimental conditions, no crystals of H°PyTeI$_4$ (**4**) could be obtained. The overall features of the newly determined structure of compound **3** at 100 K (Figure S5) strictly recall those previously reported, displaying a T-shaped geometry at a 10–Te–3 hypercoordinate tellurium atom, rotated by about 46° with respect to the pyridinium ring. Similar to what was discussed above for compound **2**, chalcogen···halogen ChB and HB interactions (C–Te···I and N–H···I, respectively; Table 1) are responsible for the supramolecular packing. Contrary to what was reported in the discussion of the crystal structure collected at 298 K,[28] no significant I···I contacts were envisaged in the structure collected at 100 K, the shortest I···I distance [I···I$^{iii}$; 4.2103(2); $^{iii}$ = −x, 1−y, 1−z] being even larger than the sum of iodine vdW radii (about 4.0 Å). The Raman spectrum of compound **3** can be interpreted due to the similarities with the vibrational spectral features of the symmetric $[I_3]^{-}$ anion. In fact, the spectrum, previously reported,[28] showed an intense peak due to the symmetric stretching mode of the linear I–Te–I system at 115 $cm^{-1}$ and a very weak one, assigned to the asymmetric stretching mode, at 156 $cm^{-1}$.

Two different reaction products were isolated from $CH_2Cl_2$/*n*-hexane mixtures containing **L2** and $Br_2$, depending on the adopted molar ratio (Scheme 1). When the reaction was carried out in a 1:2 **L2**/$Br_2$ molar ratio, red block-shaped crystals suitable for X-ray diffraction analysis were grown by slow evaporation of a portion of the reaction mixture. The nature of the obtained compound was elucidated by elemental analysis and single-crystal X-ray diffraction to consist of the zwitterion H°PyTeBr$_2$ (**5**; Scheme 1). The crystal structure, previously reported,[28] shows two crystallographically independent units in the asymmetric unit, each displaying slightly different torsion angles of the Br–Te–Br moiety with respect to the 2-pyridine plane [16.3(2) and 4.7(2)°, respectively]. ChBs responsible for the solid-state intermolecular interactions are summarized in Table 1. The Raman spectrum was again dominated by the peak due to the symmetric stretching mode of the symmetric linear Br–Te–Br systems (reported at 161 $cm^{-1}$).[28]

When a large excess of dibromine was adopted (5:1), block-shaped yellow crystals were obtained and structurally characterized.[40] X-ray diffraction analysis unambiguously showed that the obtained crystals consist of the zwitterion H°PyTeBr$_4$ (**6**; Scheme 1, Figure 5, Tables S1 and S4). The Te$^{IV}$ atom displays a distorted pentacoordination with the pyridinium moiety disposed axially and the four bromide ions completing a square-pyramidal arrangement. The C–Te bond length [2.173(3) Å] is slightly longer than those reported for 1*H*-pyridine-2-tellurenyl dihalides H°PyTeCl$_2$, **3**, and **5**, [2.141(3),[21] 2.137(4) Å,[28] and 2.139(2), respectively] and very close to the corresponding bond distance determined for compound **4** (2.182 Å).[28] This confirms the nature of single bond for C–Te in aryltellurenyl halides. As in the case of compound **4**,[28] the heterocycle in compound **6** is twisted so to bisect the square defined by the four bromide ions, therefore preventing the formation of any intramolecular HB with the pyridinium N–H group. The four Te–Br distances are close to each other, ranging between 2.642(1) and 2.683(1) Å. The crystal packing results from a combination of HB and ChB interactions (Table 1). The bromine atom of the longest Te1–Br3 bond is engaged in a bent intermolecular HB with the N–H

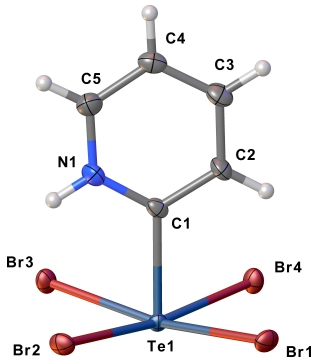


**Figure 5.** Ellipsoid plot and atom labelling scheme of compound **6**. Thermal ellipsoids were drawn at the 50% probability level. Selected interatomic distances, angles, and dihedrals: C1–Te1, 2.173(3); Te1–Br1, 2.642(1); Te1–Br2, 2.681(1); Te1–Br3, 2.683(1); Te1–Br4, 2.664(1) Å; C1–Te1–Br1, 86.3(1); C1–Te1–Br2, 85.5(1); C1–Te1–Br3, 84.3(1); C1–Te1–Br4, 86.4(1); Br1–Te1–Br3, 170.63(4); Br2–Te1–Br4, 171.80(4); N1–C1–Te1–Br1, 47.0(5); N1–C1–Te1–Br2, 43.9(5)°.

pyridinium of a symmetry related unit. The Te atom is in turn involved in a bifurcated ChB with the Br1$^{ii}$ and Br2$^{ii}$ atoms of a different zwitterionic unit to form a supramolecular motif that propagates along the *c*-axis (Table 1 and Figure 6).

The FT-Raman spectrum of compound **6** shows a structured peak at 160–170 cm$^{-1}$ derived from two clearly distinguishable components with maxima at 157 and 168 cm$^{-1}$, respectively (Figure 7). The two overlapping peaks may be tentatively attributed to the $\sigma_g$ symmetric stretching vibrations ($\nu_{symm}$) of the two linear orthogonal nonequivalent Br2–Te1–Br4 and Br3–Te1–Br1 (10–Te–3) three-body systems. The weak peak at 251 cm$^{-1}$ can be assigned to the antisymmetric stretching mode ($\nu_{asymm}$), while the structured peak in the 80–100 cm$^{-1}$ region to the bending vibrational modes ($\nu_b$). A comparison of $\nu_{symm}$ values recorded in the Raman spectra for the Br–Br–Br, Br–Se–Br, and Br–Te–Br groups isolated in $[Br_3]^-$,[30,51] and compounds **2**, **5**–**6**, respectively, clearly shows the common nature of the corresponding 10–Ch–3 three-body systems, which is reflected in the almost identical wavenumber of symmetric stretching vibrations (falling between 160 and 168 cm$^{-1}$).

## DFT Theoretical Calculations

### *Bond Analysis*

Selected metric parameters for **L1**, **L2**, and all pyridin-2-ylchalcogenyl mono-, di-, and tetra-halides, including those not currently reported in the literature (see below), at the DFT-optimized (mPW1PW functional,[52] def2-TZVP[53] basis sets)[54] geometries are summarized in Table S5.

A comparison of optimized and structural data, available for compounds **L1**,[23,55,56] **L2**,[26] **2**,[25] **3**, **4**,[28] **5**, and **6** showed an excellent agreement at the selected level of theory (Table S6 and Figure S6). In particular, the optimized chalcogen-chalcogen bond lengths in **L1** and **L2** were calculated to be 2.349 (average structural distance in the two known polymorphs, 2.30 Å)[23–56] and 2.723 Å (structural distance, 2.656 Å)[26] for Ch = Se and Te, respectively. The potential energy surface (PES) of compounds **L1** and **L2** was investigated to verify the preferential conformations of the two compounds. The PES as a function of the mutual rotation of the pyridine substituents shows a low rotational barrier ($\Delta E < 12$ kcal/mol). Contrary to what was found for diphenyldiselane, where the maxima in the PES were found for the periplanar and antiperiplanar conformations ($\Delta E = 7.3$ and 5.3 kcal/mol, respectively),[11] in the case of **L1** and **L2**, the less stable conformation was found when the two substituents are facing each other ($\tau = 0.0°$ in Figure S7) while the conformations with the orthogonal pyridine rings ($\tau \approx 90.0°$) and the antiperiplanar one ($\tau = 180.0°$) show very similar potential energy values. This suggests that the conformation assumed by H**L1**$^+$ in compound **1**, which is energetically unfavored in **L1**, is HB-stabilized by the N···H···N system, as previously discussed. A second-order perturbation (SOPT) analysis of the Fock matrix in the natural bonding orbital (NBO)[57,58,59] basis showed that the stabilization of the antiperiplanar conformation ($\tau = 180.0°$ in Figure S7) can be partly attributed to a charge-transfer (CT) between the lone pair of electrons (LP) located on the nitrogen atom of the pyridine ring to the antibonding NBO localized on the Ch–Ch bond. The energy of this weak interaction increases on passing from Ch = Se to Ch = Te (amounting to 0.9 and 2.0 kcal/mol, respectively). In both **L1** and **L2**, the rotational barrier around the Ch–Ch bond is low, amounting to 11.7 and 10.4 kcal/mol, respectively. Although never isolated as monomers, pyridin-2-ylchalcogenyl halides °PyChX have been shown to be effective chalcogenocyclization agents when reacted with olefins and acetylene derivatives[21] in polar [3 + 2] cycloadditions.[60,61,62] The geometry optimized for the four model monomers °PyChX (Ch = Se, Te; X = Br, I) shows very similar structural features, with a C–Ch–X angle in the range 99.4–103.7° (Table S5) and C–Ch and Ch–X single bonds (Wiberg[63] bond indices WBI in the range 0.02–1.00 and 0.97–1.02, respectively; Table S7). The fully planar structure was found as the most stable conformation. Nevertheless, a PES scan shows a very low rotational barrier ($\Delta E < 4$ kcal/mol; Figure S8) of the Ch–X group with respect to the pyridine plane. The bond lengths and angles optimized for °PyTeBr and °PyTeI (Table S5) can be compared with the metric parameters determined for the corresponding dimers, although the C–Te and Te–X bond lengths and C–Te–X bond angle (X = Br, I)[28,29] in the dimers are necessarily perturbed by the N→Te interactions [X = Br: C–Te, 2.125(2) Å; Te–Br, 2.7059(3) Å; C–Te–Br, 87.98(6)°; X = I: average C–Te, 2.129 Å; Te–I, 2.839 Å; C–Te–I, 92.21°]. The Kohn-Sham (KS) HOMO and LUMO of pyridin-2-ylchalcogenide halides are $\pi^*$ and $\sigma^*$ molecular orbitals (MOs), respectively, which are mainly localized on the Ch–X fragment (Figure S9 for °PySeBr). The negative natural

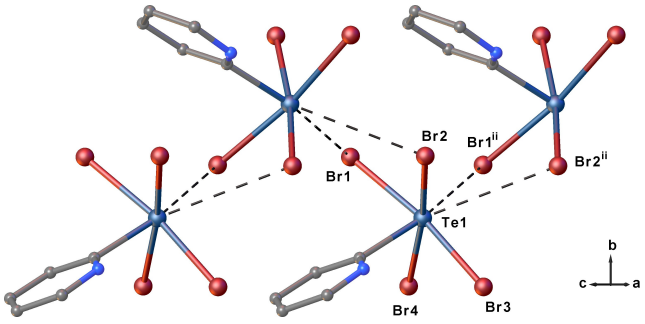


**Figure 6.** Portion of the crystal packing of compound **6** seen along [101] direction showing C–Te···Br ChB interactions. Hydrogen atoms were omitted for clarity. Symmetry operation: $^{ii}$ = x, 3/2−y, −1/2+z.

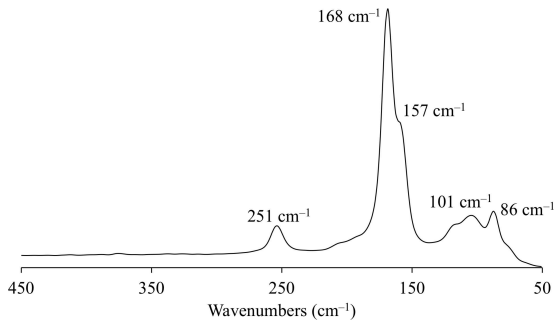


**Figure 7.** Solid-state FT-Raman spectrum (450–50 cm$^{-1}$) recorded at r.t. for compound **6**.

charge on the N atom and the positive charge on the Ch atom in the monomers °PyChX (Table S7), together with their frontier molecular orbital composition, point to the former atom as a nucleophilic center and the latter as an electrophilic center capable of accepting electron density along the Ch–X direction. This nicely accounts for the formation of both the dimers (with N→Ch–X interactions) and the dihalides (formally deriving by a $X^-$→Ch–X interaction, see below) in terms of a CT process involving the transient monomers as intermediates. In this context, it is worth noting that the structural features and the electronic structure of the chalcogenyl monohalides closely remind those of the $[R–Ch–X]^+$ cations proposed by Husebye and coworkers[64] and investigated by some of the authors[32,36,42,65,66] as hypothetical intermediates in the reactions of N-substituted (benzo)imidazole-2-chalcogenone and thiazole-2-chalcogenone R=Ch with dibromine and diiodine. The natural charge distribution on the hypothetical model cations $[R–Ch–X]^+$, which shows a σ*-LUMO localized along the Ch–X bond strictly similar to that of °PyChX monomers,[65] was invoked to systematically predict the nature of the final products, including CT "spoke" and hypercoordinate T-shaped adducts as well as dications containing a Ch–Ch bond. As described above, from the reactions of **L1**/**L2** with $Br_2$/$I_2$, the T-shaped dihalides **2**, **3**, and **5** were obtained, featuring the 10–Ch–3 linear moiety. The crystal structures of these dihalides show the propeller-like X–Ch–X group rotated by different angles with respect to the pyridinium plane, ranging between 4.7 and 64° in compounds **5** and **2**,[25,28] respectively, suggesting a low rotational barrier around the C–Ch bond. Accordingly, a PES scan shows that for all H°PyChX$_2$ compounds the planar conformer is the most stable one in the gas phase, but that the conformer with the $ChX_2$ linear moiety perpendicular to the pyridinium is only 6–12 kcal/mol higher in energy (Figure S10).

The stabilization of the planar isomer in the gas phase can be at least partly attributed to an intramolecular N–H···X HB interaction, whose strength increases on passing from Ch=Te to Se, and from X=Br to I (Wiberg bond indices, $WBI_{H···X}$: Ch=Se, X=Br, 0.144; Ch=Se, X=I, 0.148; Ch=Te, X=Br: 0.126; Ch=Te, X=I, 0.135) and can be evaluated by means of a SOPT analysis as the sum of LP(X)→BD*(N–H) contributions ($E_{CT}$: Ch=Se, X=Br, 18.6; Ch=Se, X=I, 32.6; Ch=Te, X=Br: 31.4; Ch=Te, X=I, 28.8 kcal/mol). The HB interaction is systematically reflected in a remarkable elongation (in the range 5%–9%) of the optimized Ch–X bond lengths on the same side as the NH group (Table S5) with respect to the opposite one. This asymmetry induces a slight but remarkable difference in the charge on the two terminal halides, the one on the same side as the NH group being more negatively charged. In the solid state, the intramolecular HB compete with different intermolecular HB and ChB interactions (Table 1). Accordingly, the N–H···X intramolecular interaction, which was not envisaged in the crystal structures of compounds **2**–**6**, was experimentally confirmed in the case of H°PyTeCl$_2$,[21] whose single crystal X-ray diffraction analysis demonstrated that the *quasi*-planar structure [τ=4.7(1) °] was stabilized by a strong N–H···Cl HB,[21] similar to that reported for benzothiazole-2-selone-dichloride.[67] All X–Ch–X moieties in dihalides H°PyChX$_2$ can be qualitatively considered as three-body systems, whose bond can be described according to the Rundle-Pimentel (RP) MO model of 3c–4e σ-bonded systems,[68,69] each Ch–X bond having an ideal bond order of 0.5. In particular as regards compound **2** (Figure S11), the σ-bonding MO $\psi^b$ corresponding tothe in-phase combination of $p_z$ atomic orbitals (AOs) can be identified as the occupied KS-MO #65 (HOMO-8), the nonbonding combination $\psi^{nb}$ as the occupied KS-MO #72 (HOMO-1), and the antibonding out-of-phase combination $\psi^*$ of $p_z$ AOs as the virtual KS-MO #75 (LUMO+1). In agreement with the RP description, Wiberg bond indices calculated for the two Ch–X bonds of chalcogenyl dihalides ($WBI_{Ch–X}$) range between 0.424 and 0.668, the differences between $WBI_{Ch–X}$ of the two bonds of a X–Ch–X moiety being due to the asymmetry discussed above. The sum of the WBIs for the two opposite Ch–X bonds is in the range between 1.07 (Ch=Se, X=I) and 1.12 (Ch=Te, X=Br), i.e. extremely close to the unity value expected for an ideal 3c–4e three-body system. The DFT calculations were extended to H°PyChX$_4$ tetrahalides (Ch=Se, Te; X=Br, I). The metric parameters optimized for tetrahalides (Table S5) are in agreement with the corresponding available structural data (see above). As discussed for the dihalides, a partial asymmetry of the Ch–X bond distances was calculated in the optimized structures (with bond lengths differing by 5%–8%; Table S5), and hence in the negative natural charges calculated on the X atoms (Table S7). Compared to the corresponding dihalides, an increased positive charge on the chalcogen atom, reflecting the increase in the formal oxidation state, and more negative charges on the halogen atoms result in an augmented polarization of Ch–X bonds. An examination of KS-MO and WBIs calculated for H°PyChX$_4$ tetrahalides confirms that the $ChX_4$ moiety is ideally composed of two orthogonal 3c–4e X–Ch–X systems. Indeed, the sum of WBI calculated on each X–Ch–X linear moiety falls in the range between 1.00 and 1.15, and the composition of KS-MOs is consistent with that expected based on the RP 3c–4e model. In particular, taking as an example compound **6** (Figure 8), the bonding combinations $\psi_1^b$ and $\psi_2^b$ of $p_z$ AOs can be envisaged in MOs #90 and #91 and the antibonding combinations $\psi_1^*$ and $\psi_2^*$ in MO #106 and MO #107, for the Br–Te–Br system on the same plane and that orthogonal to the pyridinium ring, respectively. The symmetry-allowed sum

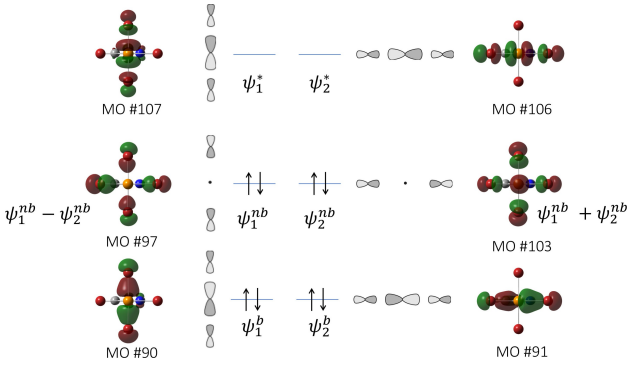


**Figure 8.** Isosurfaces of the KS-MOs (left and right) involved in the 3c–4e bond description (center) of the two orthogonal 10–Te–3 Br–Te–Br three-body systems in compound **6** at the optimized geometry. Cutoff value = 0.05 |e|. Hydrogen atoms were omitted for clarity.

$\psi_1^{nb} + \psi_2^{nb}$ and difference $\psi_1^{nb} - \psi_2^{nb}$ of the nonbonding combinations of AOs belonging to the two orthogonal Br–Te–Br systems can be clearly spotted in MO #103 and MO #97, respectively.

### *Computational Thermochemistry*

DFT calculations were extended to the calculation of the bond dissociation energy (BDE) of **L1** and **L2**, evaluated by thermochemical calculations[70] ($T$ = 298.15 K; Table S8). The suitability of the computational setup adopted was validated by calculating the BDE of diethyldisulfide ($Et_2S_2$) taken as a model compound. The BDE value calculated for $Et_2S_2$ (59.46 kcal/mol) is in excellent agreement with the corresponding values calculated at the DFT level by Guo *et al.* [functional: Boese-Martin for kinetics, BMK;[71] basis sets: 6-311G(d,p); 59.48 kcal/mol][72] and close to the value recently reported by Yang *et al.* [functional: M06-2X;[73] basis sets: 6-311++G(2df,2p); 65.7 kcal/mol].[74] The BDE value calculated for **L3** (57.98 kcal/mol) confirms that the chalcogen-chalcogen BDEs are marginally modulated by the nature of the substituents.[72,75] The BDE value calculated for **L1** (51.5 kcal/mol) is very close to the theoretical values reported for $Me_2Se_2$ and $Et_2Se_2$ (56.41 and 51.94 kcal/mol, respectively)[72] and to the experimental value determined for $Me_2Se_2$ and $Bu_2Se_2$ (45.9 and 50.4 kcal/mol, respectively).[76] The BDE calculated for **L2** (45.5 kcal/mol) can be compared with the experimental values reported for $Bu_2Te_2$ (35.6 kcal/mol).[76] These calculations show a clear trend in the BDEs decreasing from disulfides, to diselanes and ditellanes, which is reflected in an opposite trend in the propensity of dichalcogenides to undergo a cleavage of the chalcogen-chalcogen bond. Notably, the endothermic cleavage of the Ch–Ch bond is a key step in the reactions of dichalcogenides $R_2Ch_2$ with dihalogens $X_2$ to give chalcogenyl halides RChX. Therefore, a larger BDE of the Ch–Ch bonds prevents the formation of chalcogenyl halides and stronger oxidizing dihalogens are required. Accordingly, the reactions of bis(pyridin-2-yl)dichalcogenides $^{o}Py_2Ch_2$ with the less oxidizing dihalogen $I_2$ did not lead to the cleavage of the Ch–Ch bond when Ch = S and Se (**L3** and **L1**, respectively), whereas the cleavage of the chalcogen-chalcogen bond was systematically observed when Ch = Te (**L2**) or the more oxidizing dibromine was adopted as an oxidizing agent (Scheme 1).

To investigate these reactions further, the reaction enthalpy $\Delta H_{r1}$ and free energy values and $\Delta G_{r1}$ associated with the oxidation reactions (1):

$$^{1}/_{2}\ ^{o}Py_2Ch_2 + {}^{1}/_{2}\ X_2 \rightarrow {}^{o}PyChX \quad (1)$$

were calculated at 298.15 K for all combinations of Ch = Se, Te and X = Br, I (Table S9) from the relevant thermochemical data calculated for each reagent and product. An analysis of $\Delta H_{r1}$ and $\Delta G_{r1}$ values (Table S9) shows that in the gas phase the reaction is more hexoergonic i) when X = Br and ii) when Ch = Te, i.e. according to the oxidizing ability of the dihalogen ($Br_2 > I_2$) and the tendency of the bis(pyridin-2-yl)dichalcogenides to undergo a Ch–Ch cleavage ($BDE_{L1} > BDE_{L2}$). $\Delta G_{r1}$ for reaction (1) range between −2.7 and −13.6 kcal/mol according to the series:

$^{o}PySeI > {}^{o}PyTeI > {}^{o}PySeBr > {}^{o}PyTeBr$

The formation of dihalides $H^{o}PyChX_2$ from monohalides, according to reaction (2) is always thermodynamically favored (Table S9):

$$^{o}PyChX + HX \rightarrow H^{o}PyChX_2 \quad (2)$$

The $\Delta H_{r3}$ and $\Delta G_{r3}$ values were calculated for the oxidation reaction (3):

$$H^{o}PyChX_2 + X_2 \rightarrow H^{o}PyChX_4 \quad (3)$$

where the following trend of decreasing $\Delta G_{r3}$ was calculated (Table S9):

$H^{o}PySeI_4 > H^{o}PySeBr_4 > H^{o}PyTeI_4 > H^{o}PyTeBr_4$

Interestingly, negative values of $\Delta H_{r3}$ and $\Delta G_{r3}$ were calculated only for the formation of compound **6** ($\Delta G_{r3}$ = −16.4 kcal/mol), while a remarkably positive value (23.6 kcal/mol) was calculated for $H^{o}PySeI_4$. Although these gas-phase calculations regarding the formation reactions of $^{o}PyChX$ and $H^{o}PyChX_4$ should not be overemphasized and cannot be directly correlated to the corresponding reactions in solution, it is worth noting that:

1) Thermodynamic state functions calculated for reaction (1) show a negligibly negative $\Delta G_{r1}$ value (−2.7 kcal/mol) for the diiodine oxidation of **L1**. This is consistent with i) the isolation of compound **1**, where **L1** was protonated without Se–Se cleavage; ii) the absence of any report on the species $H^{o}PySeI_2$ (Scheme 1) in the literature available to date.
2) $\Delta G_{r3}$ values calculated for reaction (3) suggest that the formation of tetrahalides derived from **L1** is not thermodynamically favored. Indeed, to date $H^{o}PySeBr_4$ and $H^{o}PySeI_4$ have not been reported in the literature and have not been isolated experimentally (Scheme 1), even when a large excess of the corresponding dihalogen was adopted.
3) With the sole exception of $H^{o}PySeI_4$, negative $\Delta H_r$ values were calculated for the formation of all $H^{o}PyChX_2$ [reaction (2)] and $H^{o}PyChX_4$ [reaction (3)] halides. Hence, the unfavored reactions should not be attributed to an intrinsic instability of the chalcogenyl halides whose formation was not observed, but rather to negative $\Delta S_r$ reaction entropy values of the oxidation reactions involved in their formation.

### *DFT Analysis of secondary interactions*

Structural analysis of the compounds obtained from the reactions of **L1**/**L2** with $I_2$/$Br_2$ and characterized by single-crystal X-ray diffraction (see above) revealed that their crystal packing is governed by a combination of HB, XB, and ChB interactions (Table 1). XB and ChB are defined as net attractive interactions R–X/Ch···A between a XB/ChB donor (R = heteroatom, metal ion, organic group) and an acceptor A.[39,77,78,79] XB and ChB are considered to belong to the σ-hole family of intermolecular interactions.[80,81] This type of interaction is governed by the anisotropy of the electrostatic potential at the interacting atoms, the depletion of which (σ-hole), indicating an electrophilic region

of positive potential on the X/Ch atom, is typically disposed opposite to the covalent R–X or R–Ch bond of the donor group for XB and ChB, respectively. Recently, the non-covalency of σ-hole interactions has been severely criticized.[82,83] Indeed, energy decomposition analyses (EDAs) have shown that the energy of σ-hole interactions can be decomposed into an electrostatic term and an MO-mixing term,[83,84] and that dispersion effects[85] also play an often fundamental role.[79,86,87] The relative contribution of each term largely depends on the nature of the involved interaction groups, so that the nature of σ-hole interactions ranges from almost purely ionic to largely covalent. The mapping of the electrostatic potential topology, highlighting electrophilic (positive or less negative potential) regions on R–X/Ch and nucleophilic regions (negative potential) on A, combined with the study of antibonding (BD*) NBOs on the R–X/Ch bond and LPs on the A group, allows the electrostatic and MO-mixing nature of ChB and XB interactions to be investigated at DFT level.[35]

Single-crystal X-ray diffraction analysis carried out on compound **1** showed that XB interactions are responsible for the infinite polyiodide network discussed above. The $I^-\cdots I_2$ interactions, which are essentially of the same nature as those reported for $[(\mathbf{HL3}^+)(I^-)\cdot 5/2I_2]_\infty$, were previously commented on based on DFT calculations.[33] The monoprotonated cation is involved in ChB interactions (Table 1 and Figure 1a and Figure S2). In Figure S12a the map of the molecular electrostatic potential (MEP) calculated for the cation $\mathbf{HL1}^+$ at the molecular geometry found in the crystal structure is depicted. Each selenium atom of the cation displays two σ-holes (less positive potential, shown in red in Figure S12a) associated to different orthogonal regions of more positive potential (shown in blue in Figure S12a), in accordance with the formation of the linear C–Se···Se ChB interactions depicted in Figure 1a. On the other hand, the interaction geometry is consistent with a Se→Se–C CT interaction involving the LPs of electrons on the Se atoms and the σ*-$BD^*_{C-Se}$-NBOs on each C–Se bond (Figure S12b). The orientation of the LPs nicely accounts for the C1–Se1···I6$^{ii}$ interactions (Table 1), while the composition of the σ*-$BD^*_{Se-Se}$, localized on the diselane bond (Figure S13), is in perfect agreement with the geometry of the Se2–Se1···I3$^{iv}$ and Se1–Se2···I4 ChB interactions (Table 1 and Figure S2).

A comparison of the MEP mapped on the electron density surface for $H^oPyChX_2$ and $H^oPyChX_4$ (Figure S14a and Figure 9a for compounds **3** and **6**, respectively) shows similar features for the two classes of halides, with σ-holes on the Ch atoms disposed opposite to the C–Ch bonds and a belt of negative potential around each halogen terminal atom. This clearly explains the C–Ch···X–Ch interacting geometries (Table 1), which show almost linear C–Ch···X and bent Ch···X–Ch fragments [compound **2**: C–Se···Br 172.49(9), Se···Br–Se 107.87(1)°; compound **3**: C–Te···I 171.31(6), Te···I–Te 143.35(1)°; compound **4**: C–Te···I 149.6, Te···I–Te 100.4°; compound **5**: C–Te···Br 177.98(6) and 178.17(6), Te···Br–Te 90.68(1) and 90.15(1)°; compound **6**: C–Te···Br 150.3(1) and 149.9(1), Te···Br–Te 100.07(3) and 100.84(3)°]. The C–Te ChB donor ability is reflected in the composition of the σ*-in-nature antibonding BD* that is localized on the C–Ch bond of the chalcogenyl moiety (Figure S14b and Figure 9b for compounds **3** and **6**, respectively).

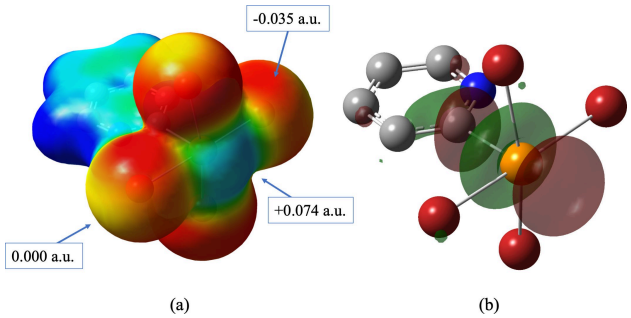


**Figure 9.** (a) Molecular electrostatic potential mapped on the electron density [$5\cdot10^{-3}$ | e | /Bohr$^3$; range −0.035 (red) to +0.100 (blue) a.u.] and (b) isosurface of the BD*-NBO localized on the C–Te bond (cutoff value = 0.05 | e |) calculated for compound **6** at the DFT level. Hydrogen atoms were omitted for clarity.

## Conclusions

In this paper we have studied the reactivity of bis(pyridin-2-yl)diselane (**L1**) and ditellane (**L2**) towards $I_2$ and $Br_2$. In the framework of these reactions, typically originating zwitterionic 1*H*-pyridine-2-chalcogenyl halides as a consequence of the oxidative cleavage of the Ch–Ch bond, an exception is represented by compound **1**. In this compound the monoprotonated cation $\mathbf{HL1}^+$ templates an authentic infinite three-dimensional polyiodide network governed by $I_2\cdots I^-$ interactions all shorter than 3.6 Å. Several chalcogenyl halides have been reported previously. In this work we have recollected at 100 K the structural data for the already known compound **3**, while the new compound **6** was isolated and structurally characterized, thus completing the potential products resulting from these reactions. Notably, all chalcogenyl di- and tetra-halides are zwitterionic species, the negative charge of the $Ch^{II}X_2$ / $Ch^{IV}X_4$ fragments being counterbalanced by the protonated 2-pyridinium substituent.

The experimental results described in this work, paralleled by thermochemical DFT calculations, allow a better understanding of the main factors influencing the outcome of these reactions. In particular, it is worth noting that the absence of any report on the species $H^oPySeI_2$, $H^oPySeBr_4$, and $H^oPySeI_4$ in the literature is justified by the positive or only slightly negative Gibbs free energy values of the corresponding formation reactions. All the reported dihalides and tetrahalides contain X–Ch–X three body-systems: the structural evidence and DFT calculations clearly show the analogy with the T-shaped oxidative adducts $R{=}ChX_2$ obtained from the reactions of substituted (benzo)imidazole-2-chalcogenone and (benzo)thiazole-2-chalcogenone with $Br_2$ and $I_2$. Both in $R{=}ChX_2$ hypercoordinate adducts and $H^oPyChX_n$ ($n = 2$, 4) zwitterions, the linear X–Ch–X moieties can be considered as 3c–4e systems, whose electronic structure can be qualitatively described according to the Rundle-Pimentel model. The three-body system nature of these fragments, common also to the

$[I_2 \cdot I]^-$ building blocks constituting the polyiodide network in compound **1**, is reflected in the similarities of their FT-Raman spectra, all showing the typical intense $\sigma_g$ symmetric stretching mode ($\nu_{symm}$) in the region 150–170 $cm^{-1}$ for Br–Ch–Br and at about 110 $cm^{-1}$ for I–Ch–I systems, independently of the nature of the central Ch atom.

All the systems examined in this work show intermolecular interactions that clearly fall in the realm of halogen- (XB) and chalcogen-bonds (ChB). Neglecting dispersion effects, for these sister interactions two concurrent interpretation models have been proposed, i.e. a MO-mixing approach, consisting of a partial charge-transfer from a nucleophile (Lewis base) to an electrophile (Lewis acid), or a noncovalent σ-hole interpretation based on the topology of electrostatic potential. Many authors, by means of energy decomposition schemes, have shown that both aspects contribute to XB and ChB interactions. In the limited selection of zwitterionic systems dealt with in this work, it is clearly shown that the two models converge to the same conclusions, the depletion areas of electrostatic potential (σ-holes) being topologically related to the direction of antibonding natural orbitals.

Notably, the same computational approach adopted for investigating the redox reactivity of chalcogenyl halides and their propensity to form secondary interactions could be exported to different dichalcogenide derivatives showing biological activities.

## Experimental Section

### Materials and Methods

Reagents were used as purchased without further purification. Melting points are uncorrected and were determined on a FALC mod. C (up to 290 °C) melting point apparatus. Elemental analyses were performed with a CHNS/O PE 2400 series II CHNS/O elemental analyzer ($T = 925$ °C). FT-IR spectra (Figures S15–S17) were recorded with a Thermo-Nicolet 5700 spectrometer at room temperature: KBr pellets with a KBr beam splitter and KBr windows (4000–400 $cm^{-1}$, resolution 4 $cm^{-1}$) were used. FT-Raman spectra were recorded with a resolution of 4 $cm^{-1}$ on a Bruker RFS100 FT-Raman spectrometer, fitted with an In–Ga-As detector (room temperature) operating with a Nd:YAG laser (excitation wavelength 1064 nm), with a 180° scattering geometry.

### X-ray Diffraction Measurements

Single-crystal X-ray diffraction data for compound **1** were collected using a Rigaku Saturn724 diffractometer operating at 125 K, and using Mo *Kα* radiation.[40] Data for compounds **3** and **6** were collected at 100 K and 293 K, respectively, on a XtaLAB AFC12 diffractometer using a rotating anode Mo *Kα* X-ray source.[40] For compound **6**, all the screened crystals were twinned, and an appropriate twin law has therefore been applied to the refinement, lowering R1 from 3.22% to 1.85%. The diffraction pattern featured some satellite peaks suggesting a weak modulation that was taken into account by integrating the data using the parent unit cell, then modelling the modulation as disorder to obtain a reliable approximate solution. The minor positions of the tellurium and bromine atoms (~2.5%) have been modelled isotropically (with their thermal parameters constrained to be the same and refined together) and with geometric parameter restraints. Please note that it was not possible to locate the minor positions of the pyridine atoms (C1 > C5 and N1) in the election difference map. The pyridine atoms have therefore been modelled using single sites with thermal parameters restraints. The locations of all hydrogen atoms could be determined from the electron difference map, however their positions were calculated and refined using riding models, otherwise they refined to unrealistic geometries. Data collection and processing for these structures were carried out using CrysAlisPro 1.171.40.29a or 1.171.41.93a (Rigaku Oxford Diffraction, 2020).[88] The structures were solved with the ShelXT[89] 2018 solution program using dual-space algorithms and by using Olex2 1.5[90] as the graphical interface. The models were refined with ShelXL[91] 2018 using full matrix least squares minimization on $F^2$.

### Theoretical Calculations

The computational investigation was carried out at the DFT level[54] by adopting the Gaussian 16[92] suite of programs. Following the results of previously reported calculations on related systems, the mPW1PW hybrid functional[52] was adopted, along with the full-electron triple-ζ basis sets (BSs) def2-TZVP, including polarization functions and relativistic effective core potentials (RECPs) for the heavier Te and I species.[53] BS data were extracted from the EMSL BS Library.[93] The memory required for each calculation was evaluated by the GaussMem cross-platform (Linux, macOS, Windows) program as a function of the number of shared processors, the total number of basis set functions, and a memory threshold depending on the highest angular momentum basis function. The molecular geometry optimizations (Tables S10–S25) were performed starting from structural data, when available. The nature of the minima of each optimized geometry was verified by harmonic frequency calculations. PES scans were performed by imposing the rotation around either Ch–Ch or C–Ch bonds for **L1**/**L2** and the chalcogenyl halides, respectively, and optimizing the resulting geometry at each rotational step. Theoretical gas-phase BDE were calculated as the total energy required for the homolytic breakage of the Ch–Ch bond.[70] BDE is thus the enthalpy change of the reaction:

$$^{\circ}Py_2Ch_2 \rightarrow 2\ ^{\circ}PyCh\cdot \quad (4)$$

that can be calculated from the difference of the unscaled sums of electronic and thermal enthalpies, corrected for Zero Point Energies (ZPEs), *H*, calculated for the organochalcogenyl radical and the dichalcogenide:

$$BDE = 2 \cdot H(^{\circ}PyCh\cdot) - H(^{\circ}Py_2Ch_2) \quad (5)$$

Analogously, the enthalpy and free energy variations associated with the reactions (1) and (2) were calculated as differences of thermochemical values. All thermochemical calculations were carried out at $T = 298.15$ K at the optimized geometries as a part of harmonic frequency calculations. When multiple conformers could be optimized, thermodynamic state functions refer to the most stable conformer. Charge distributions and Wiberg bond indices[63] were evaluated at the NBO level[57–59] at the optimized geometries. The programs Molden[94] and GaussView 6.0.16[95] were used to investigate the optimized structures and molecular orbital shapes.

### Synthesis

Dichalcogenides **L1** and **L2** were synthesized according to the literature.[23,26] Compounds **2**, **3**, and **5** were prepared previously according to different synthetic procedures.[25,28] In the following, the syntheses of compounds **1** and **6**, providing single crystals suitable for X-ray diffraction analysis, are reported.

### *Synthesis of $[(HL1^+)(I^-)\cdot 5/2I_2]_\infty$ (1)*

600 μL ($1.5\cdot10^{-4}$ mol) of a molecular diiodine solution (0.25 M in $CH_3CN$) were added dropwise to a solution of **L1** (15.7 mg; $5.0\cdot10^{-5}$ mol in 4 mL of $CH_3CN$) while stirring. The resulting solution was stirred at room temperature for 20 min, filtered through a 0.45 μm PTFE filter and the solvent left to slowly evaporate. Black crystals were isolated, gently washed with petroleum ether and air dried (20.4 mg; $1.9\cdot10^{-5}$ mol; 38%). M. p. = 78 °C; Elemental analysis calcd (%) for $C_{10}H_9N_2Se_2I_6$: C 11.16, H 0.84, N 2.60. Found: C 11.58, H 0.32, N 2.37. FT-Raman (600–50 $cm^{-1}$, 50 mW, 100 scans): 178(1.8), 165(10.0), 153(8.0), 111(1.5) $cm^{-1}$ (relative intensities, strongest = 10). FT-IR (KBr, 4000–400 $cm^{-1}$): 3122w, 3070w, 3030w, 1637w, 1610ms, 1583s, 1544mw, 1473m, 1450ms, 1439s, 1425s, 1406ms, 1385m, 1315mw, 1277mw, 1246mw, 1155mw, 1107w, 1064w, 1047mw, 1010s, 964w, 762vs, 696mw, 636ms, 470ms $cm^{-1}$.

### *Synthesis of $H^oPyTeBr_4$ (6)*

**L2** (10.3 mg; $2.5\cdot10^{-5}$ mol) was dissolved in 4 mL of $CH_2Cl_2$. The vial was then transferred in a diffusion chamber containing a dibromine solution in *n*-hexane ($3.0\cdot10^{-2}$ M, 4 mL, $1.2\cdot10^{-4}$ mol) and kept at room temperature for 48 h. The product was obtained as yellow block-shaped crystals suitable for X-ray diffraction analysis. The crystals were carefully transferred on a Petri dish, washed with petroleum ether and air dried (18.5 mg; $3.5\cdot10^{-5}$ mol; 71%). M. p. = 159 °C dec. Elemental analysis calcd (%) for $C_5H_5NTeBr_4$: C 11.41, H 0.96, N 2.66. Found: C 11.37, H 0.78, N 2.54. FT-Raman (600–50 $cm^{-1}$, 50 mW, 100 scans): 251(1.5), 168(10.0), 157(5.1), 116(1.7), 99(1.8), 86(2.0) $cm^{-1}$ (relative intensities, strongest = 10). FT-IR (KBr, 4000–400 $cm^{-1}$): 3076br, 2777ms, 2424mw, 1628mw, 1599ms, 1577s, 1516s, 1466m, 1435s, 1361m, 1298m, 1232mw, 1465mw, 1080m, 1010m, 1009m, 966w, 885w, 823mw, 725s, 459ms $cm^{-1}$.

## Supporting Information

Crystallographic data, FT-Raman and FT-IR spectra, and DFT studies.

## *Acknowledgements*

CINECA is kindly acknowledged for providing computational resources (ISCRA C projects BIFluoex, LithoDFT, QMPhosph). KKB is thankful to NASI for the Platinum Jubilee Fellowship and UGC - New Delhi for financial assistance.

## *Conflict of Interests*

The authors declare no conflict of interest.

## *Data Availability Statement*

The data that support the findings of this study are available from the corresponding author upon reasonable request.

**Keywords:** dichalcogenide · halogen · Raman · Chalcogen Bonding · Halogen Bonding · DFT

[1] G. Kedarnath, V. K. Jain, *Coord. Chem. Rev.* **2013**, *257*, 1409–1435.
[2] M. Ibrahim, W. Hassan, D. F. Meinerz, M. dos Santos, C. V. Klimaczewski, A. M. Deobald, M. S. Costa, C. W. Nogueira, N. B. V. Barbosa, J. B. T. Rocha, *Mol. Cell. Biochem.* **2012**, *371*, 97–104.
[3] L. Orian, S. Toppo, *Free Radical Biol. Med.* **2014**, *66*, 65–74.
[4] C. Santi, C. Tidei, C. Scalera, M. Piroddi, F. Galli, *Curr. Chem. Biol.* **2013**, *7*, 25–36.
[5] C. Santi, F. Marini, E. J. Lenardão, Organoselenium Compounds in Biology and Medicine, Royal Society of Chemistry, Cambridge, 2017, pp. 35–76.
[6] D. Bartolini, J. Commodi, M. Piroddi, L. Incipini, L. Sancineto, C. Santi, F. Galli, *Free Radical Biol. Med.* **2015**, *88*, 466–480.
[7] X. Ren, Y. Xue, K. Zhang, J. Liu, G. Luo, J. Zheng, Y. Mu, J. Shen, *FEBS Lett.* **2001**, *507*, 1873–3468.
[8] L. Wang, S. Lv, G. Yan, G. Luo, Y. Mu, *Environ. Toxicol. Pharmacol.* **2010**, *30*, 1–4.
[9] D. F. Meinerz, J. Allebrandt, D. O. Mariano, E. P. Waczuk, F. A. Soares, W. Hassan, J. B. T. Rocha, *PeerJ* **2014**, *2*, e290.
[10] M. Bortoli, M. Dalla Tiezza, C. Muraro, G. Saielli, L. Orian, *Molecules* **2019**, *24*, 1250.
[11] V. Nascimento, P. Silva Cordeiro, M. Arca, F. Marini, L. Sancineto, A. L. Braga, V. Lippolis, M. Iwaoka, C. Santi, *New J. Chem.* **2020**, *44*, 9444–9451.
[12] T. Zincke, *Chem. Ber.* **1911**, *44*, 769–771.
[13] Y. V. Torubaev, A. V. Pavlova, A. A. Pasynskii, A. Raghuvanshi, M. M. Shaikh, *Russ. J. Coord. Chem.* **2015**, *41*, 638–643.
[14] S. S. dos Santos, E. S. Lang, G. Manzoni de Oliveira, *J. Organomet. Chem.* **2007**, *692*, 3081–3088.
[15] E. S. Lang, G. Manzoni de Oliveira, R. Marceli Fernandez Jr, E. M. Vázquez-López, *Inorg. Chem. Commun.* **2003**, *6*, 869–872.
[16] N. W. Alcock, W. D. Harrison, *Acta Crystallogr.* **1982**, *B38*, 2677–2679.
[17] S. S. dos Santos, E. S. Lang, R. A. Burrow, *J. Braz. Chem. Soc.* **2006**, *17*, 1566–1570.
[18] M. C. Aragoni, M. Arca, A. J. Blake, E. Cadoni, L. O. Copolovici, F. Isaia, V. Lippolis, S. Murgia, A. M. Pop, C. Silvestru, J. P. Tidey, R. A. Varga, *New J. Chem.* **2019**, *43*, 11821–11831.
[19] E. S. Lang, G. A. Casagrande, G. Manzoni de Oliveira, G. Nanci Ledesma, S. S. Lemos, E. E. Castellano, U. Abram, *Eur. J. Inorg. Chem.* **2006**, 958–964.
[20] A. J. Z. Londero, N. R. Pineda, V. Matos, P. C. Piquini, U. Abram, E. S. Lang, *J. Organomet. Chem.* **2020**, *929*, 121553.
[21] V. N. Khrustalev, Z. V. Matsulevich, J. M. Lukiyanova, R. R. Aysin, A. S. Peregudov, L. A. Leites, A. V. Borisov, *Eur. J. Inorg. Chem.* **2014**, 3582–3586.
[22] V. N. Khrustalev, Z. V. Matsulevich, R. R. Aysin, J. M. Lukiyanova, G. K. Fukin, Y. V. Zubavichus, R. K. Askerov, A. M. Maharramov, A. V. Borisov, *Struct. Chem.* **2016**, *27*, 1733–1741.
[23] C. O. Kienitz, C. Thöne, P. G. Jones, *Inorg. Chem.* **1996**, ***35***, 3990–3997.
[24] A. Toshimitsu, H. Owada, K. Terao, S. Uemura, M. Okano, *J. Org. Chem.* **1984**, *49*, 3796–3800.
[25] Z. V. Matsulevich, J. M. Lukiyanova, V. I. Naumov, G. N. Borisova, V. K. Osmanov, A. V. Borisov, M. M. Grishina, V. N. Khrustalev, *Acta Crystallogr.* **2019**, *E75*, 675–679.
[26] K. K. Bhasin, V. Arora, T. M. Klapötke, M. .-J. Crawford, *Eur. J. Inorg. Chem.* **2004**, 4781–4788.
[27] A. V. Borisov, Z. V. Matsulevich, V. K. Osmanov, G. N. Borisova, B. I. Naumov, G. Z. Mammadova, A. M. Maharramov, V. M. Khrustalev, V. V. Kachala, *Russ. Chem. Bull.* **2012**, *61*, 91–94.
[28] F. D. da Silva, C. A. D. P. Simões, S. S. dos Santos, E. S. Lang, *Chem. Select* **2017**, *7*, 2708–2712.
[29] I. V. Buslov, A. S. Novikov, V. N. Khrustalev, M. V. Grudova, A. S. Kubasov, Z. V. Matsulevich, A. V. Borisov, J. M. Lukiyanova, M. M. Grishina, A. A. Kirichuk, T. V. Serebryanskaya, A. S. Kritchenkov, A. G. Tskhovrebov, *Symmetry* **2021**, *13*, 2350.
[30] M. C. Aragoni, M. Arca, F. A. Devillanova, M. B. Hursthouse, S. L. Huth, F. Isaia, V. Lippolis, A. Mancini, G. Verani, *Eur. J. Inorg. Chem.* **2008**, 3921–3928.
[31] M. C. Aragoni, M. Arca, F. A. Devillanova, M. B. Hursthouse, S. L. Huth, V. Lippolis, A. Mancini, H. R. Ogilvie, G. Verani, *J. Organomet. Chem.* **2005**, *690*, 1923–1934.

[32] M. C. Aragoni, M. Arca, F. Demartin, F. A. Devillanova, A. Garau, F. Isaia, V. Lippolis, G. Verani, *Dalton Trans.* **2005**, 2252–2258.
[33] M. C. Aragoni, M. Arca, F. A. Devillanova, M. B. Hursthouse, S. L. Huth, F. Isaia, V. Lippolis, A. Mancini, *CrystEngComm* **2004**, *6*, 540–542.
[34] F. Isaia, M. C. Aragoni, M. Arca, C. Caltagirone, C. Castellano, F. Demartin, A. Garau, V. Lippolis, A. Pintus, *Dalton Trans.* **2011**, *40*, 4505–4513.
[35] M. C. Aragoni, M. Arca, C. Caltagirone, C. Castellano, F. Demartin, P. G. Jones, T. Pivetta, E. Podda, V. Lippolis, S. Murgia, G. Picci, *J. Org. Chem.* **2022**, *87*, 15448–15465.
[36] M. C. Aragoni, M. Arca, F. A. Devillanova, P. Grimaldi, F. Isaia, F. Lelj, V. Lippolis, *Eur. J. Inorg. Chem.* **2006**, 2166–2174.
[37] M. C. Aragoni, M. Arca, F. A. Devillanova, F. Isaia, V. Lippolis, *Cryst. Growth Des.* **2012**, *2*, 2769–2779.
[38] M. C. Aragoni, M. F. Cherchi, V. Lippolis, A. Pintus, E. Podda, A. M. Z. Slawin, J. D. Woollins, M. Arca, *Molecules* **2022**, *27*, 6289.
[39] M. C. Aragoni, M. Arca, V. Lippolis, A. Pintus, Y. Torubaev, E. Podda, *Molecules* **2023**, *28*, 3133.
[40] Deposition Numbers 2297030 (for compound **1**), 2297028 (for compound **3**), and 2297029 (for compound **6**) contain the supplementary crystallographic data for this paper. These data are provided free of charge by the joint Cambridge Crystallographic Data Centre and Fachinformationszentrum Karlsruhe Access Structures service.
[41] M. C. Aragoni, E. Podda, M. Arca, A. Pintus, V. Lippolis, C. Caltagirone, R. H. Bartz, E. J. Lenardão, G. Perin, R. F. Schumacher, S. J. Coles, J. B. Orton, *New J. Chem.* **2022**, *46*, 21921–21929.
[42] E. L. Rimmer, R. D. Bailey, W. T. Pennington, T. W. Hanks, *J. Chem. Soc. Perkin Trans. 2* **1998**, 2557–2562.
[43] C. Horn, M. Scudder, I. Dance, *CrystEngComm* **2001**, *3*, 9–14.
[44] H. Svensson, L. L. Kloo, *Chem. Rev.* **2003**, *103*, 1649–1684. .
[45] M. C. Aragoni, M. Arca, F. Demartin, F. A. Devillanova, A. Garau, F. Isaia, V. Lippolis, S. Rizzato, G. Verani, *Inorg. Chim. Acta* **2004**, *357*, 3803–3809.
[46] A. J. Blake, R. O. Gould, S. Parsons, C. Radek, M. Schröder, *Angew. Chem. Int. Ed. Engl.* **1995**, *34*, 2374–2376.
[47] K. F. Tebbe, R. Buchem, *Z. Anorg. Allg. Chem.* **1998**, *624*, 671–678.
[48] F. van Bolhuis, P. B. Koster, T. Migchelsen, *Acta Crystallogr.* **1967**, *23*, 90–91.
[49] A. J. Blake, F. A. Devillanova, R. O. Gould, W. .-S. Li, V. Lippolis, S. Parsons, C. Radek, M. Schröder, *Chem. Soc. Rev.* **1998**, *27*, 195–206.
[50] C. W. Perkins, J. C. Martin, A. J. Arduengo, W. Lau, A. Alegria, J. K. Kochi, *J. Am. Chem. Soc.* **1980**, *102*, 7753–7759.
[51] M. C. Aragoni, M. Arca, S. J. Coles, F. A. Devillanova, M. B. Hursthouse, S. L. Huth, F. Isaia, V. Lippolis, A. Mancini, *CrystEngComm* **2011**, *13*, 6319–6322.
[52] C. Adamo, V. Barone, *J. Chem. Phys.* **1998**, *108*, 664–675.
[53] F. Weigend, R. Ahlrichs, *Phys. Chem. Chem. Phys.* **2005**, *7*, 3297–3305.
[54] W. Koch, M. C. Holthausen, A chemist's guide to density functional theory, Wiley-VCH, New York, 2001.
[55] J. Romero, M. L. Durán, J. A. García-Vázquez, A. Castiñeiras, A. Sousa, L. Christiaens, J. Zubieta, *Inorg. Chim. Acta* **1997**, *255*, 307–311.
[56] S. Dunne, E. von Nagy-Felsobuki, M. Mackay, *Acta Crystallogr.* **1998**, *C54*, 887–889.
[57] A. E. Reed, R. B. Weinstock, F. Weinhold, *J. Chem. Phys.* **1985**, *83*, 735–746.
[58] A. E. Reed, F. Weinhold, *J. Chem. Phys.* **1985**, *83*, 1736–1740.
[59] A. E. Reed, L. A. Curtiss, F. Weinhold, *Chem. Rev.* **1988**, *88*, 899–926.
[60] R. R. Schmidt, *Angew. Chem. Int. Ed. Engl.* **1973**, *12*, 212–224.
[61] C. K. Bradsher, *Adv. Heterocycl. Chem.* **1974**, *16*, 289–324.
[62] A. R. Katritzky, M. A. C. Button, *J. Org. Chem.* **2001**, *66*, 5595–5600.
[63] K. B. Wiberg, *Tetrahedron* **1968**, *24*, 1083–1096.
[64] M. D. Rudd, S. V. Lindeman, S. Husebye, *Acta Chem. Scand.* **1997**, *51*, 689–708.
[65] M. C. Aragoni, M. Arca, F. Demartin, F. A. Devillanova, A. Garau, F. Isaia, F. Lelj, V. Lippolis, G. Verani, *Chem. Eur. J.* **2001**, *7*, 3122–3133.
[66] M. C. Aragoni, M. Arca, A. J. Blake, F. A. Devillanova, W. .-W. du Mont, A. Garau, F. Isaia, V. Lippolis, G. Verani, C. Wilson, *Angew. Chem. Int. Ed. Engl.* **2001**, *40*, 4229–4232.
[67] V. N. Khrustalev, S. R. Ismaylova, R. R. Aysin, Z. V. Matsulevich, V. K. Osmanov, A. S. Peregudov, A. V. Borisov, *Eur. J. Inorg. Chem.* **2012**, 5456–5460.
[68] G. C. Pimentel, *J. Chem. Phys.* **1951**, *19*, 446–448.
[69] R. E. Rundle, *J. Am. Chem. Soc.* **1947**, *69*, 1327–1331.
[70] N. Q. Trung, A. Mechler, N. T. Hoa, Q. V. Vo, *R. Soc. Open Sci.* **2022**, *9*, 220177.
[71] A. D. Boese, J. M. L. Martin, *J. Chem. Phys.* **2004**, *121*, 3405–3416.
[72] Y. Guo, S. R. Alvarado, J. D. Barclay, J. Vela, *ACS Nano* **2013**, *7*, 3616–3626.
[73] Y. Zhao, D. G. Truhlar, *Theor. Chem. Acc.* **2008**, *120*, 215–241.
[74] Y. .-M. Yang, H. .-Z. Yu, X. .-H. Sun, Z. .-M. Dang, *J. Phys. Org. Chem.* **2016**, *29*, 6–13.
[75] R. L. Brutchey, *Acc. Chem. Res.* **2015**, *48*, 2918–2926.
[76] V. I. Tel'noi, M. S. Sheiman, *Russ. Chem. Rev.* **1995**, *64*, 309–316.
[77] G. Cavallo, P. Metrangolo, R. Milani, T. Pilati, A. Priimagi, G. Resnati, G. Terraneo, *Chem. Rev.* **2016**, *116*, 2478–2601.
[78] J. Y. C. Lim, P. D. Beer, *Chem.* **2018**, *4*, 731–783.
[79] M. Arca, G. Ciancaleoni, A. Pintus, A. Computational Methods to Study Chalcogen Bond, in "Chalcogen Chemistry: fundamentals and applications", V. Lippolis, C. Santi, E. J. Lenardão, A. L. Braga eds, RSC publishing, UK, **2022**, 476–493, and references therein.
[80] P. Metrangolo, F. Meyer, T. Pilati, G. Resnati, G. Terraneo, *Angew. Chem.* **2008**, *47*, 6114–6127.
[81] E. Navarro-García, B. Galmés, M. D. Velasco, A. Frontera, A. Caballero, *Chem. Eur. J.* **2020**, *26*, 4706–4713.
[82] F. Winhold, *Molecules* **2023**, *28*, 3776.
[83] L. de Azevedo Santos, S. C. C. van der Lubbe, T. A. Hamlin, T. C. Ramalho, F. M. Bickelhaupt, *ChemistryOpen* **2021**, *10*, 391–401.
[84] V. Oliveira, E. Kraka, D. Cremer, *Phys. Chem. Chem. Phys.* **2016**, *18*, 33031–33046.
[85] L. N. Anderson, F. W. Aquino, A. E. Raeber, X. Chen, B. M. Wong, *J. Chem. Theory Comput.* **2018**, *14*, 180–190.
[86] W. Dong, Q. Li, S. Scheiner, *Molecules* **2018**, *23*, 1681.
[87] A. Bauzá, A. Frontera, *ChemPhysChem* **2020**, *21*, 26–31.
[88] CrysAlis PRO. Agilent Technologies Ltd, Yarnton, Oxfordshire, England, **2014**.
[89] G. M. Sheldrick, *Acta Crystallogr.* **2015**, *A71*, 3–8.
[90] O. V. Dolomanov, L. J. Bourhis, R. J. Gildea, J. A. K. Howard, H. Puschmann, *J. Appl. Crystallogr.* **2009**, *42*, 339–341.
[91] G. M. Sheldrick, *Acta Crystallogr.* **2015**, *C71*, 3–8.
[92] Gaussian 16, Rev. C.01, M. J. Frisch, G. W. Trucks, H. B. Schlegel, G. E. Scuseria, M. A. Robb, J. R. Cheeseman, G. Scalmani, V. Barone, G. A. Petersson, H. Nakatsuji, X. Li, M. Caricato, A. V. Marenich, J. Bloino, B. G. Janesko, R. Gomperts, B. Mennucci, H. P. Hratchian, J. V. Ortiz, A. F. Izmaylov, J. L. Sonnenberg, D. Williams-Young, F. Ding, F. Lipparini, F. Egidi, J. Goings, B. Peng, A. Petrone, T. Henderson, D. Ranasinghe, V. G. Zakrzewski, J. Gao, N. Rega, G. Zheng, W. Liang, M. Hada, M. Ehara, K. Toyota, R. Fukuda, J. Hasegawa, M. Ishida, T. Nakajima, Y. Honda, O. Kitao, H. Nakai, T. Vreven, K. Throssell, J. A. Montgomery, Jr., J. E. Peralta, F. Ogliaro, M. J. Bearpark, J. J. Heyd, E. N. Brothers, K. N. Kudin, V. N. Staroverov, T. A. Keith, R. Kobayashi, J. Normand, K. Raghavachari, A. P. Rendell, J. C. Burant, S. S. Iyengar, J. Tomasi, M. Cossi, J. M. Millam, M. Klene, C. Adamo, R. Cammi, J. W. Ochterski, R. L. Martin, K. Morokuma, O. Farkas, J. B. Foresman, and D. J. Fox, Gaussian, Inc., Wallingford CT, 2016.
[93] B. P. Pritchard, D. Altarawy, B. Didier, T. D. Gibson, T. L. Windus, *J. Chem. Inf. Model.* **2019**, *59*, 4814–4820.
[94] G. Schaftenaar, J. Noordik, *J. Comput.-Aided Mol. Des.* **2000**, *14*, 123–134.
[95] R. D. Dennington, T. A. Keith, J. M. Millam, GaussView 6.0. 16, Semichem; Inc., Shawnee Mission KS, **2016**.

Manuscript received: September 23, 2023
Revised manuscript received: October 12, 2023
Accepted manuscript online: October 16, 2023
Version of record online: ■■, ■■

# RESEARCH ARTICLE

The reactions between bis(pyridin-2-yl)diselane $^{o}Py_2Se_2$ and ditellane $^{o}Py_2Te_2$ ($^{o}Py$ = pyridyn-2-yl) and $I_2/Br_2$ lead to a variety of products including $\{[H(^{o}Py_2Se_2)^+](I^-)\cdot 5/2I_2\}_\infty$, showing an infinite polyiodide network, and several zwitterionic chalcogenyl di- and tetra-halides, such as $H^{o}PySe^{II}Br_2$, $H^{o}PyTe^{II}I_2$, and $H^{o}PyTe^{IV}Br_4$. The nature of all the reaction products was elucidated by means of XRD analysis, FT-Raman spectroscopy and DFT calculations.

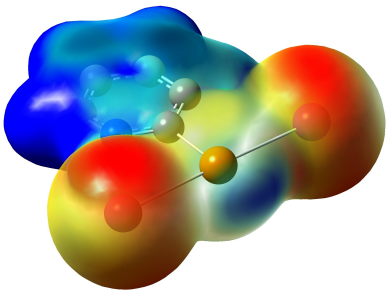

*Prof. Dr. M. C. Aragoni, Dr. E. Podda, Dr. S. Chaudhary, Dr. A. K. K. Bhasin, Prof. Dr. K. K. Bhasin, Prof. Dr. S. J. Coles, Dr. J. B. Orton, Prof. F. Isaia, Prof. Dr. V. Lippolis, Dr. A. Pintus, Prof. Dr. A. M. Z. Slawin, Prof. Dr. J. D. Woollins, Prof. Dr. M. Arca**

1 – 13

**An Experimental and Theoretical Insight into $I_2/Br_2$ Oxidation of Bis(pyridin-2-yl)Diselane and Ditellane**